2-2008

Over-Ocean Validation of the Global Convective Diagnostic

David W. Martin
University of Wisconsin - Madison

Richard A. Kohrs
University of Wisconsin - Madison

Frederick R. Mosher
Embry-Riddle Aeronautical University, moshe774@erau.edu

Carlo Maria Medaglia
Italian National Research Council - Institute of Atmospheric Sciences and Climate

Claudia Adamo
Italian National Research Council - Institute of Atmospheric Sciences and Climate

Over-Ocean Validation of the Global Convective Diagnostic

DAVID W. MARTIN AND RICHARD A. KOHRS

Space Science and Engineering Center, University of Wisconsin—Madison, Madison, Wisconsin

FREDERICK R. MOSHER

Applied Aviation Sciences, Embry-Riddle Aeronautical University, Daytona Beach, Florida

CARLO MARIA MEDAGLIA AND CLAUDIA ADAMO

Institute of Atmospheric Sciences and Climate, Italian National Research Council, Rome, Italy

(Manuscript received 28 June 2006, in final form 17 May 2007)

ABSTRACT

The global convective diagnostic (GCD) is a bispectral (infrared and water vapor), day–night scheme for operationally mapping deep convection by means of geostationary satellite images. This article describes a test of GCD performance over tropical and subtropical waters near North America. The test consists of six cases, each involving a convective cloud complex. A seventh case treats convection over land. For each case, a map of deep convection was constructed from image pairs from *Geostationary Operational Environmental Satellite-12* (*GOES-12*). Case by case and for all maritime cases together, the GCD map was compared with a convective parameter derived from the radar on the Tropical Rainfall Measuring Mission (TRMM), a polar-orbiting satellite. In general, each GCD map showed a bloblike feature. In each case, the radar convective pixels typically fell within the GCD blob. However, (except for the land case) the GCD predicted far too many convective pixels. In the maritime cases overprediction was reduced (without correspondingly impairing other measures of performance) by lowering the nominal GCD threshold. With this adjustment in place, for the six maritime cases taken individually, the GCD tended to yield more consistent results than did a monospectral (infrared) convective scheme. With the cases combined, at the lower threshold the GCD performed somewhat better than one of the more stable versions of the infrared scheme. Comparison with lightning events (also observed by TRMM) suggests the possibility of future improvement to the GCD through the incorporation of geostationary satellite observations of lightning.

1. Introduction

Cumulonimbus clouds (cbs) interest several communities. Numerical modelers must represent the transport of mass (including water in its various forms) in cumulonimbus updrafts. Physical meteorologists seek information on the role of cbs in maintaining the global electric circuit. The heights of cbs within a convective region may yield information on the height of the tropopause and on exchange of air between the troposphere and stratosphere (Schmetz et al. 1997; Tjemkes et al. 1997). Validation of the U.S. National Weather Service Aviation Weather Center's "high-level significant weather forecasts" requires information on cb location. Turbulence (e.g., Lane et al. 2003) and icing make the cb a special concern of aviation (Brennan 1983).

Radars operating in the millimeter-to-centimeter-wavelength band constitute the preferred tool for monitoring cbs (i.e., observing them day and night). However, earth curvature limits the ranges of individual radars and cost constrains the deployment of networked radars. As a practical matter, ground-based radars can monitor convective activity only over and near land areas.

Weather satellites offer a method of monitoring cbs over the oceans. Each of the geostationary weather satellites has a window-infrared (11 μm) channel. Operating in a transparent region of the infrared spectrum, the

Corresponding author address: David W. Martin, Space Science and Engineering Center, 1225 West Dayton St., Madison, WI 53706.
E-mail: dave.martin@ssec.wisc.edu

DOI: 10.1175/2007JAMC1525.1

window-infrared (IR) channel is designed to sense the surface or cloud-top temperature. In the usual case, a group of cbs in any particular IR image can be isolated through some cold threshold temperature. However, a threshold picked to isolate every cb at times also will unfortunately flag thick (but convectively inert) cirrus clouds (Ebert et al. 1996; Mapes and Houze 1993). Furthermore, a threshold optimized for one region or season may not work well in other regions or seasons (e.g., Adler et al. 1985; Lau et al. 1991; Zhang 1993).

Each of the geostationary weather satellites also has a water-vapor (WV; 6.7 μm) channel. Operating in a region of the infrared spectrum dominated by WV absorption, the WV channel is designed to sense moisture in the middle and upper troposphere. Because the low-latitude troposphere and midlatitude troposphere cool with height, ordinarily an IR brightness temperature will be warmer than a collocated WV brightness temperature (Fritz and Laszlo 1993; Tjemkes et al. 1997). However, as noted by Fritz and Laszlo (1993), Ackerman (1996), Schmetz et al. (1997), and Tjemkes et al. (1997), sometimes a WV brightness temperature exceeds the matching IR brightness temperature. In all midlatitude and tropical cases documented so far (Fritz and Laszlo 1993; Ackerman 1996; Kurino 1997), the warm WV pixel occurred at a low IR brightness temperature (never more than 245 K). Tjemkes et al. (1997) termed the phenomenon "warm water vapor pixel."

A warm WV pixel could originate in a noisy sensor or in coarse digitization of a signal (Ottenbacher and Schmetz 1994), as well as through bias in a calibration (Ackerman 1996; Tjemkes et al. 1997; Schmetz et al. 1997). It might occur through an offset in the registration of the WV and IR pixels (Ottenbacher and Schmetz 1994), through viewing geometry (the limb darkening effect; Ackerman 1996; Tjemkes et al. 1997), or through the effect of the (nonlinear) Planck function on broken cold cloud (Ackerman 1996; Schmetz et al. 1997). Although each of these several factors may contribute to the occurrence of a particular warm WV pixel, it seems none can account for the body of warm WV pixels found in satellite images. A warm WV pixel could also result from differential cloud emissivity (WV less than IR; Ottenbacher and Schmetz 1994). Ackerman (1996) does not rule out such a cause; however, Szejwach (1982) and Liou et al. (1990) both found effectively constant cirrus emissivities in WV and IR bands.

Through simulations, Tjemkes et al. (1997) explained the phenomenon of the warm WV pixel in terms of a spectrally black cloud in an atmosphere characterized by temperature lapse (cooling with height) below the tropopause and temperature inversion above [i.e., in the stratosphere; also see Fritz and Laszlo (1993)]. A satellite radiometer operating in the IR band receives radiation in proportion to the temperature of the (spectrally black) cloud top. In the WV band, moisture in the atmosphere above the cloud top modulates radiation from the cloud top. As the top of this cloud rises toward the tropopause, radiation at the satellite declines more rapidly in the IR band than in the WV band. With the cloud top at some distance below the tropopause, brightness temperatures equalize. If the cloud top continues to rise, the WV brightness temperature might exceed the IR brightness temperature.

Together with their geographic distribution, the association of warm WV pixels with cold IR pixels led Fritz and Laszlo (1993), Ackerman (1996), and Tjemkes et al. (1997) to suggest an origin in deep convective cloud.[1] This association prompted Schmetz et al. (1997) to propose the use of warm WV pixels to monitor deep convection. In 2001, Mosher suggested that the IR − WV temperature difference could be used as a real-time indicator of convective weather hazards around the globe for aircraft operations (Mosher 2001). A year later, on a trial basis, he implemented this idea as the global convective diagnostic (GCD; Mosher 2002).

Operating at a pixel in a bispectral image received from an operational geostationary satellite, the GCD algorithm calculates the difference between brightness temperatures in IR and WV bands. Let T_b be brightness temperature. Superscripts ir and wv refer to, respectively, the window-infrared and WV bands. Then, the brightness temperature difference is given by

$$\delta T_b \equiv T_b^{\mathrm{ir}} - T_b^{\mathrm{wv}}. \tag{1}$$

The GCD is defined in terms of δT_b:

$$\text{If} \quad \delta T_b < 1\ \mathrm{K} \quad \text{then} \quad \mathrm{GCD} = 1, \quad \text{else} \quad \mathrm{GCD} = 0. \tag{2}$$

The value 1 represents deep convective cloud. By repeating this calculation for all pixels in the image pair, the algorithm constructs a map of deep convection.

Focusing on tropical and subtropical waters, we describe a small, blind test of the GCD. The test treats

[1] In separate schemes Ba and Gruber (2001) and Kuligowski (2002) each used the IR − WV brightness temperature difference to distinguish raining and nonraining categories of cold pixel in image data of the U.S. geostationary satellites. Kurino (1997) used the same variable as one of three factors in a rainfall scheme tailored to the Japanese geostationary satellites.

images from two satellites: *Geostationary Operational Environmental Satellite-12* (*GOES-12*)[2] and the Tropical Rainfall Measuring Mission (TRMM). GCD is mapped from *GOES-12*. Through its precipitation radar (PR) and Lightning Imaging Sensor (LIS), TRMM provides independent mappings of deep convection. The test addresses three questions. First, how well does the GCD discriminate between maritime cbs and other maritime clouds? Second, does the GCD perform better than a "benchmark" index? Third, can performance be improved by reducing the temperature-difference threshold?

2. Data

a. GCD (GOES-12)

In the case of the *GOES-12* imaging instrument, superscripts wv and ir refer, respectively, to bands 3 and 4. Band 3 peaks near 6.7 μm; band 4 peaks near 11 μm. Real-time and archived multispectral *GOES-12* image data were made available through the ingest process of the "Space Science and Engineering Center desktop ingestor" (SDI). Calibrated and navigated *GOES-12* data were serviced and processed using applications within the Man–Computer Interactive Data Access System (McIDAS; Lazzara et al. 1999). For band 3, a one-count change in the (10 bit) calibrated data corresponds to a 0.35-K change in brightness temperature; for band 4, it correspondes to a 0.11-K change in brightness temperature (Weinreb et al. 2006). Both changes refer to a scene at 300 K.[3]

b. Validation

Validation data for any test of the GCD must map deep convection. For our particular test, the mapping must cover tropical parts of the western Atlantic Ocean and the eastern Pacific Ocean. It must also at least occasionally coincide with scans from the *GOES-12* imager.

At the time of the study, TRMM orbited Earth every 90 min at an inclination of 35°. The PR, one of five instruments on the TRMM, scanned a swath that was 247 km wide. At the subpoint of the satellite, a scan spanned 5.0 km. Along a beam, at range increments of 250 m, the radar measured reflectivity from the surface to an altitude of at least 15 km (Kozu et al. 2001).

Of the TRMM Science Data and Information System (TSDIS) products, algorithm 2A23 (TRMM PR rain characteristics, version 5) suited the requirements of this study best. The 2A23 algorithm (developed by the TRMM Science Team) reduces PR column reflectivities to one of two states: rain or no rain. When rain is present (with a high degree of confidence), the algorithm calculates its height. This parameter, height of storm (HS), is given in meters above mean sea level. It does not necessarily imply rain reaching the surface (J. Kwaitkowski 2004, personal communication). Inter alia, Algorithm 2A23 provides (to the nearest second) scan time and (whether raining or not) latitude and longitude of the center of each integrated field of view along a scan.

The LIS, another instrument aboard the TRMM platform, achieves a flash detection efficiency of 90% (Christian et al. 2000). Operating in a narrow band within the optical spectrum, the LIS simultaneously measures radiances at 16 384 points below the satellite. Spaced 3–6 km apart, these points compose an array 600 km on a side. The LIS repeats this measurement, or frame, every 2 ms. At a particular location beneath the satellite, the array dimension and sampling frequency together ordinarily yield a set of sequential measurements, or an observation, spanning 90 s. Thus, an observation lasts long enough to capture storms having flash rates as small as one per minute.

Christian et al. (2000) define the variable called *event* as "the occurrence of a single pixel exceeding the background threshold during a single frame."[4] Without distinction, cloud-to-cloud lightning, in-cloud lightning, and cloud-to-ground lightning are recorded. In the context of the LIS, event is a number ranging from 0 to (potentially) 45 000.

3. Method

McIDAS was used to identify cases and to acquire, display, and manipulate image data. This section describes the selection of cases and the processing of image data for each case.

[2] At the time of the test, *GOES-12* occupied the "east" position (75°W).

[3] For display purposes, the 10-bit brightness temperatures were converted to 8-bit brightness counts. The value 242 K represents a break point in this conversion. For brightness temperatures greater than 242 K, a change of 0.5 K corresponds to a change of one brightness count. For temperatures less than 242 K, a change of 1.0 K corresponds to a change of one brightness count. All figures that present GCD data draw on the 8-bit brightness temperatures.

[4] If, at a pixel, the brightness during the integration window of 2 ms exceeds a reference value then the algorithm records an event. Thus, as Christian et al. (2000) note, an event may consist of more than one lightning pulse.

TABLE 1. The cases discussed in this paper. All dates refer to 2003. The six maritime cases are listed first.

Case No.	Date	GOES scan time (UTC)		Lag (min)	Comment
		Start	Coincidence		
1	15 May	2045	2056	0	Eastern Pacific; cloud cluster
2	1 Jun	0645	0654	1	Gulf Stream/Cape Hatteras; squall line
3	5 Jun	0932	0936	1	Coastal Campeche Bay; cloud cluster
4	12 Jun	1940	1945	2	Caribbean Sea; vortical cloud
5	25 Jun	2215	2223	0	Caribbean Sea; vortical cloud
6	30 Jun	1415	1424	4	Gulf Coast; Tropical Storm Bill
7	12 Jun	0115	0127	7	Texas–Oklahoma; squall line

a. Selection of cases

Orbital geometries and scan modes assured the occasional intersection of a bundle of PR scans with a bundle of *GOES-12* scans. However, *GOES-12* scan time and scan coverage varied from hour to hour and from day to day. In the absence of a consistent relation between the TRMM orbit (hence, PR scan) and the *GOES-12* scan, each day's intersections (if any) had to be discovered individually.

Premised on geolocation errors of less than 4 km and scan-time errors of less than 0.5 min, a script was written to check a given day's SDI images for space–time coincidences between *GOES-12* and TRMM. [McIDAS uses National Oceanic and Atmospheric Administration (NOAA) two-line orbital element data to predict the location of the TRMM at any given time.] If a GOES image fell within the geographical confines of this study (5°–30°N, 45°–105°W), the script calculated the times of the first and last scans. If a TRMM orbit coincided in space and time with such an image, the investigators were alerted.

The script was run on McIDAS each day through the period 1 June–4 July 2003. McIDAS checked 4710 *GOES-12* images and sent 54 alerts. Alerts were processed in three stages. First, the set was screened. Second, the remaining alerts were ranked. Last, a domain was defined for each of the top-ranking alerts. At no point before or during this process were the TRMM data consulted.

Screening identified each "space–time coincidence." To qualify as a space–time coincidence, an alert had to meet three conditions: overlapping data of dimension ~100 km (or more), scan-time difference of not more than 7 min, and (within the space–time window) at least one active cb. The size condition was intended to assure the possibility of a statistically meaningful sample of pixels. [Expressed as an area (10^4 km^2), it falls within the range of peak (maximum) sizes in Sherwood and Wahrlich's (1999) study of mesoscale convective systems of the southwestern Pacific Ocean.] The difference condition was aimed at reducing the likelihood of a mismatch between the stage of any deep convective cell in the GOES view and the stage of that cell in the PR view. Cumulonimbus presence was determined by inspecting the relevant IR image. The application of these conditions to the set of alerts yielded 10 space–time coincidences.

Ranking ordered the space–time coincidences. It took place in two steps. First, coincidences were scored according to a set of five parameters, each referenced to the convective cell (or group of cells) captured by a particular coincidence. In order of importance, the parameters were distance (seaward) from a coastline, scan lag, intensity, size, and isolation. Here, "scan lag" means the absolute difference in scan times at the center of the convective cell. Intensity was estimated through inspection of the GOES imagery. Size refers to the dimensions of the convective storm, and isolation refers to its separation from neighboring cloud systems. Points were awarded in direct proportion to distance, intensity, size, and isolation and in inverse proportion to scan lag.

The second step involved classification of the space–time coincidences into one of four "synoptic" types: cloud cluster, vortical cloud (Frank and Johnson 1969), tropical storm, and squall line. From the top of the list downward, these types were allowed to appear in any order. However, none was allowed to repeat until all types had appeared.

From the ranked list, we chose the top six space–time coincidences for further processing. For each of them, using information in the corresponding alert, we established a domain. A domain is the latitude–longitude box that best balances overlap (in scans) and lag. It also aims to center the cb (or cbs). As "cases," these space–time coincidences are listed in Table 1. Subsequent to their selection, a seventh coincidence—here, case 1—was added to the original six coincidences. Case 1 originated in a test of the McIDAS script. It was added in part to include a Pacific Ocean convective system. Domains are mapped in Fig. 1. One of the seven cases

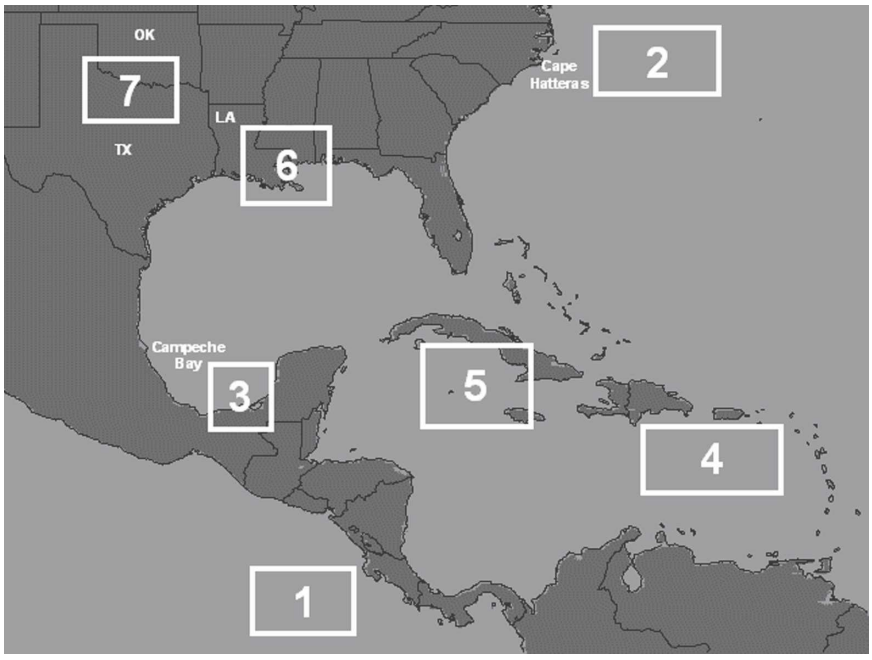

FIG. 1. Domains for the seven cases, identified by number. The states of Louisiana, Oklahoma, and Texas are marked by LA, OK, and TX, respectively.

(number 7) falls entirely over land. It is included only as a foil to the maritime cases.

b. Processing

Whatever its domain, each case was treated similarly. First, "product" images were constructed from the native images.

1) TRMM

The TSDIS orbit viewer [a visualization tool created by the Goddard Distributed Active Archive Center (DAAC)] was used to strip a text-formatted array of HS data from a (PR) 2A23 file. McIDAS applications converted the text data into McIDAS area format. Using a nearest-neighbor scheme, the HS data were remapped into a rectilinear projection of resolution 4 km × 4 km. From the remapped HS data, we created a "tower" map showing echoes that were at least 10 km

TABLE 2. Validation statistics. All range and target values are expressed in percent. Formulas for these statistics are given in appendix B.

Statistic	Variable	Range		Target
		Low	High	
"Yes" bias (i.e., forecast bias)	Bias	0	∞	100
Probability of detecting "yes" observations	POD_y	0	100	100
Probability of detecting "no" observations	POD_n	0	100	100
False-alarm rate	FAR	0	100	0
Critical success index	CSI	0	100	100
Heidke skill score	HSS	0	100	100

TABLE 3. Case-by-case values (%) of selected statistics for each of the seven band-4 thresholds. Statistics are defined in Table 2. Here, ND stands for "not defined" (i.e., division by 0).

Statistic	Threshold (K)	Case						
		1	2	3	4	5	6	Composite
POD_y	230	100	95	97	88	91	92	97
	225	100	94	96	66	85	92	96
	220	99	92	96	66	71	92	94
	215	98	88	95	66	65	92	93
	210	90	64	94	67	60	85	86
	205	60	0	89	33	37	73	64
	200	17	0	77	0	0	0	40
FAR	230	97	98	90	99	99	99	98
	225	97	98	89	99	99	99	98
	220	97	98	89	99	98	99	97
	215	96	97	89	99	94	99	96
	210	93	83	87	97	93	99	93
	205	86	ND	87	86	89	95	89
	200	73	ND	87	ND	ND	ND	86
HSS	230	1	1	10	0	0	0	1
	225	1	1	11	0	1	0	2
	220	2	2	12	1	2	1	4
	215	3	3	12	2	9	1	6
	210	9	26	15	5	13	2	12
	205	19	0	14	19	16	8	18
	200	20	0	15	0	0	0	19

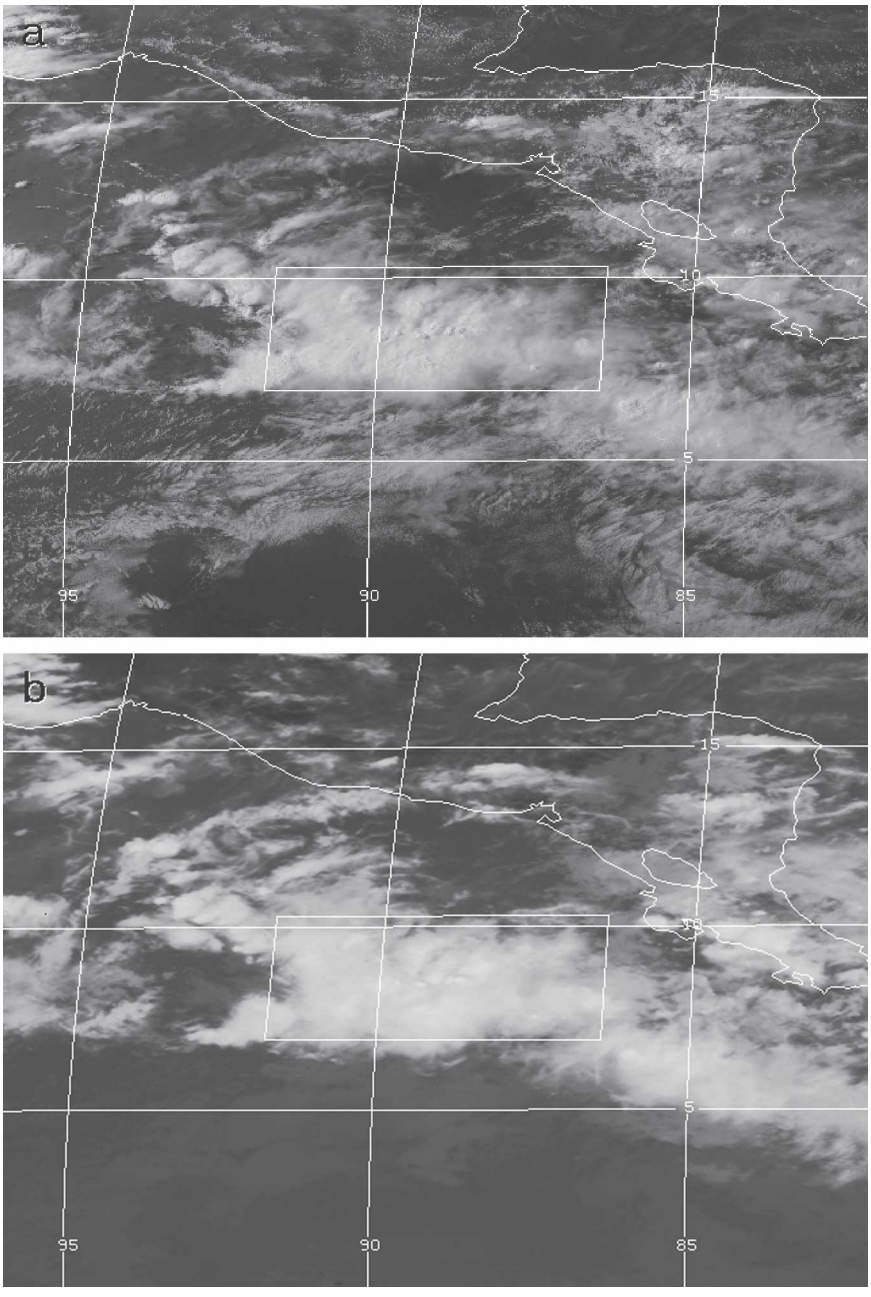

FIG. 2. GOES images for (a) visible (band 1), (b) infrared (band 4), and (c) water vapor (band 3) for case 1, 2045 UTC 15 May 2003. The box centered at 9°N, 89°W marks the domain.

tall. Except for the tower map, event data from the LIS were processed similarly.

2) GOES

Each *GOES-12* image pair (bands 3 and 4) was corrected for parallax (Wylie et al. 1998). The parallax correction assumed a 10-km cloud located at the center of the domain. Pixel by pixel, for each corrected image pair, the band-4 brightness temperature was subtracted from the band-3 brightness temperature. For display purposes, a new variable, 34DF, was defined. As δT_b ranges from -10 to 10 K, 34DF ranges from 200 to -200. Appendix A explains this transformation and relates 34DF to McIDAS brightness (hereinafter: brightness).

As with HS, brightness was remapped into a rectilinear projection of resolution 4 km $\times$ 4 km. The rectilinear brightness image then served as input to a set of

FIG. 2. (*Continued*)

seven GCD images. A GCD image in one of these sets differed from the others only in the threshold used to define a convective pixel. In units of δT_b, these thresholds were 1.0, 0.5, 0.25, 0.0, −0.25, −0.5, and −1.0 K. The threshold 1.0 K defines the "nominal" GCD (Mosher 2002). Each of the other thresholds defines an "experimental" GCD.

Except for lightning events, from each of the rectilinear images (PR as well as GOES), arrays matching the domain were extracted. These "subsected" images served as inputs for most graphical and all statistical analysis. To diagnose the performances of the GCD, we use 2 × 2 contingency tables (appendix B) and the statistics listed in Table 2. The statistics were drawn from standard (forecast) verification metrics (e.g., Mahoney et al. 2000). Each is calculated from some subset of the values contained within a contingency table, according to the formulas given in appendix B.

3) BENCHMARK INDEX (BMI)

To assess the performance of the nominal GCD, we applied a cold-temperature threshold to the band-4 image. Any image pixel that was at least as cold the threshold was assigned to the class "cb." All others were assigned to the class "not-cb."

Over the years, several temperature thresholds have been used to isolate deep convection (e.g., Fu et al. 1990; also see Mapes and Houze 1993 or Laing and Fritsch 1993). To find a threshold appropriate to the set of maritime cases (1–6), we ran the following test. Case by case, contingency tables were constructed for each of seven temperature thresholds (230, 225, 220, . . . , 200 K). This group of (6 × 7) contingency tables became the inputs for generating an equal number of sets of statistics. If they are assumed to be independent, the six cases can be combined. In the calculation of the contingency table for this "composite" case, a pixel of one case was assumed to carry the same weight as a pixel of any other case. Combining the cases led to a set of seven composite cases, one for each band-4 threshold.

Composite skill scores for the band-4 index rose monotonically with decreasing threshold temperature. They tended to peak at the colder thresholds (Table 3, right-hand column). However, at the two coldest thresholds (205 and 200 K), for one or more cases the band-4 index predicted a total absence of towers (Table 3, middle columns), even though in each case towers were present (Table 6, described below). Further, as is shown in Table 3, for two statistics (POD_y and Heidke skill score), the range (within the set of cases) increased markedly as the band-4 threshold dropped from 215 to 210 K. After considering the case-to-case stability of any particular threshold, as well as its composite skill score, we chose 215 K as a suitable threshold for a band-4 index. In Jordan's (1958) mean West Indies sounding, 215 K corresponds to a pressure of 190 hPa and a height of 12.8 km. Hereinafter, this is referred to as the benchmark index, or BMI.

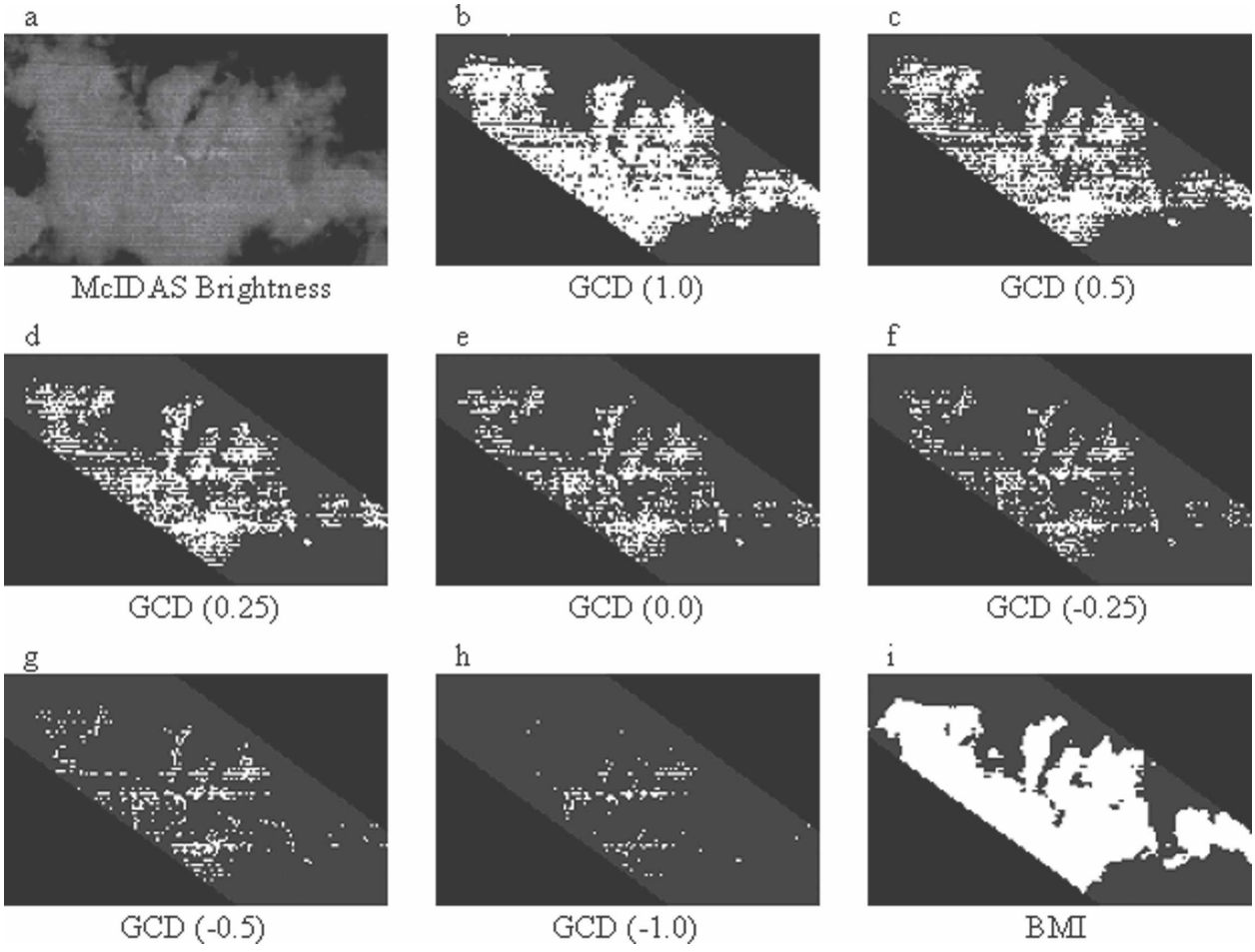

FIG. 3. Case-1 GOES image products, each in rectilinear projection, for the domain shown in Fig. 2: (a) McIDAS brightness, (b) nominal GCD, (c)–(h) experimental GCD, and (i) BMI.

4. Results

Results are presented first for two cases and then (in summary) for all cases. The first and second of the two cases ranked high and low in performance statistics, respectively.

a. Case 1

At 2056 UTC 15 May 2003, *GOES-12* scanned a large cloud cluster along the intertropical convergence zone in the eastern Pacific Ocean. The band-1 (visible) image (Fig. 2a) suggests overshooting tops within the canopy of cirrus. (A line of overshooting tops can be discerned extending eastward from the 90th meridian at 8.5°N.) Some interior structure appears in the band-4 (IR) image (Fig. 2b). *GOES-12* observed temperatures as low as 192 K. The colder (bright) spots in Fig. 2b tend to coincide with overshooting tops (shadowed bright spots in Fig. 2a). Except in lacking its contrast, the band-3 (WV) image (Fig. 2c) closely resembles the IR image.

In the brightness image (Fig. 3a), the cluster emerges from its background. Zonally oriented lines appear. The fine lines reflect noise in the band-3 and band-4 sensors (cf. Ellrod et al. 1998). The coarse lines suggest linear arrangements of convective cells. One of these lines tends to coincide with the overshooting tops noted in the band-1 image (Fig. 2a).

In the nominal GCD (Fig. 3b), we find a lobed object marked with linear (east–west) perforations. With each successive step toward the negative end of the δT_b range (Figs. 3c–h), the object shrinks and the perforations multiply. At a δT_b of -1 K (Fig. 3h), three clusters of stars remain. The stars in each cluster tend to group into lines. The strongest of these lines coincides with the cell line in the brightness image (Fig. 3a) and, hence, with the visible image's line of overshooting tops (Fig. 2a). BMI (Fig. 3i) suggests an ink blot. In position

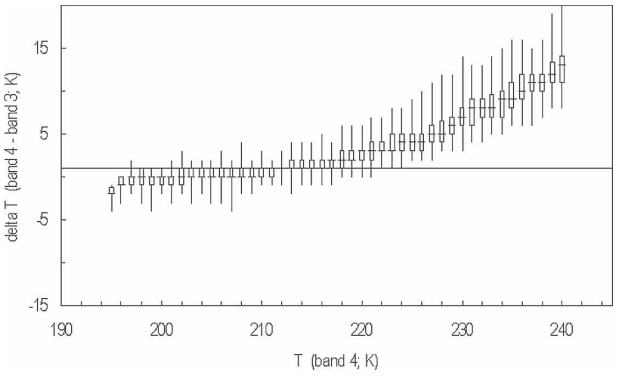

FIG. 4. Box-and-whisker plots for case 1. Each plot represents values in a "T (band 4)" (T_b^{ir}) bin of 1 K. Within a bin, the bottom and top of a box represent, respectively, the 25th and 75th quartile values of δT_b, the bar shows the median value, and the top and bottom ends of the whisker indicate, respectively, the maximum and minimum values of "delta T (band 4 − band 3)" (δT_b). The line at $\delta T_b = 1$ delineates the space occupied by the nominal GCD (below) from that outside the nominal GCD (above).

and shape (if not size), the blot resembles the nominal GCD object (Fig. 3b).

Following the method of Ackerman (1996), we compare δT_b with T_b^{ir} through box-and-whisker plots (Fig. 4). The set of plots forms a finger poking into the δT_b–T_b^{ir} space from the large-difference–warm-brightness-temperature corner of the graph. The axis of the finger (as defined by a smoothed string of median values) crosses into GCD space ($\delta T_b < 1$) near a T_b^{ir} value of 215 K. Albeit small, the slope of this axis remains positive at all temperatures below 215 K. On the other hand, a significant fraction of pixels colder than the BMI threshold (215 K) falls outside the GCD space.

The distribution of median values in Fig. 4 may be compared with those plotted by Ackerman (1996, his Fig. 8). Ackerman's pair of box-and-whisker plots draws on radiances of the High-Resolution Infrared Sounder/2 (HIRS/2) on the *NOAA-12* satellite. Separately for 2 months, they show δT_b in relation to T_b^{ir} for all pixels between the latitudes 50°S and 50°N. For both months, Ackerman's distributions extend into colder temperatures than does that of Fig. 4. Where direct comparisons are possible, his medians also tend to be colder than those of Fig. 4. Otherwise, across the interval 200–230 K, median values in Ackerman's Fig. 8 appear to fall within 1 K of those of our Fig. 4.

The HS (Fig. 5a) bears a fractal character (see Gifford 1989). The largest of the echoes contains a number of local maxima, or peaks, including four or five aligned zonally near the center of the domain. This echo lies almost entirely within the boundary of the brightness cluster (Fig. 3a). Its line of peaks nearly coincides with the cluster's line of cells. Each of the stronger peaks holds one or more tower pixels. The larger clumps of tower pixels tend to coincide with both the overshooting tops inferred from the band-1 GOES image (Fig. 2a) and the cell line in the brightness image (Fig. 3a).

To gain insight into the relationship between HS towers and δT_b, two brightness frequency distributions were constructed. (These are not shown.) One consisted of all brightness pixels; the other, called "tower brightness," consisted of just those brightness pixels associated with tower pixels. Tower brightness represented a small sample of the brightness population. This sample included most pixels brighter than 162 counts (δT_b of −2.7 K) but included no pixel darker than 98 counts (δT_b of 2.3 K).

Events (Fig. 5b) appear in two small, well-separated clusters. Within each cluster, maxima tend to lie near the center. Each of the clusters coincides with a peak in the map of HS (Fig. 5a).

Scatterplots of HS and LIS versus δT_b are shown in Figs. 6a and 6b, respectively. In the ideal case, all tall-echo points (HS > 9000–10 000 m) in the HS plot (Fig. 6a) would lie above the line $\delta T_b = 1.0$ K and all other points would lie below. The cloud of points suggests a mushroom. Except for values above roughly 11 000 m, the large-HS cap of the mushroom tilts upward with HS. Tilt in the cap indicates power in δT_b to discriminate more than one depth of deep convection. The position of the cap relative to the intersection of the 1.0-K line in δT_b and the 10 000-m line in HS suggests better performance for some members of the experimental GCD set (e.g., 0.5 K) than for the nominal GCD.

In the scatterplot of events and δT_b (Fig. 6b), the cloud of points would ideally form a wedge pointing from the high-δT_b–low-events corner to the low-δT_b–high-events corner. Figure 6b shows few events and only slight "wedging" of these events. However, most events fall within the nominal GCD space.

Table 4 gives statistics for case 1. In this table (and subsequent statistics tables), the first four rows give counts in the 2 × 2 contingency table: predicted (x) versus observed (y) (appendix B). Whether nominal or experimental, the GCD overforecasts [bias > 100 and/or false-alarm ratio (FAR) ≅ 90]. POD_y drops drastically as the δT_b threshold decreases while POD_n rises somewhat. Skill indices indicate discrimination power, especially at lower thresholds.

With respect to POD_y, BMI beats GCD across the experimental set ($\delta T_b < 1.0$ K). Otherwise, GCD performs better than BMI, although the difference in performance would have been smaller had 210 K been used as a threshold for the BMI.

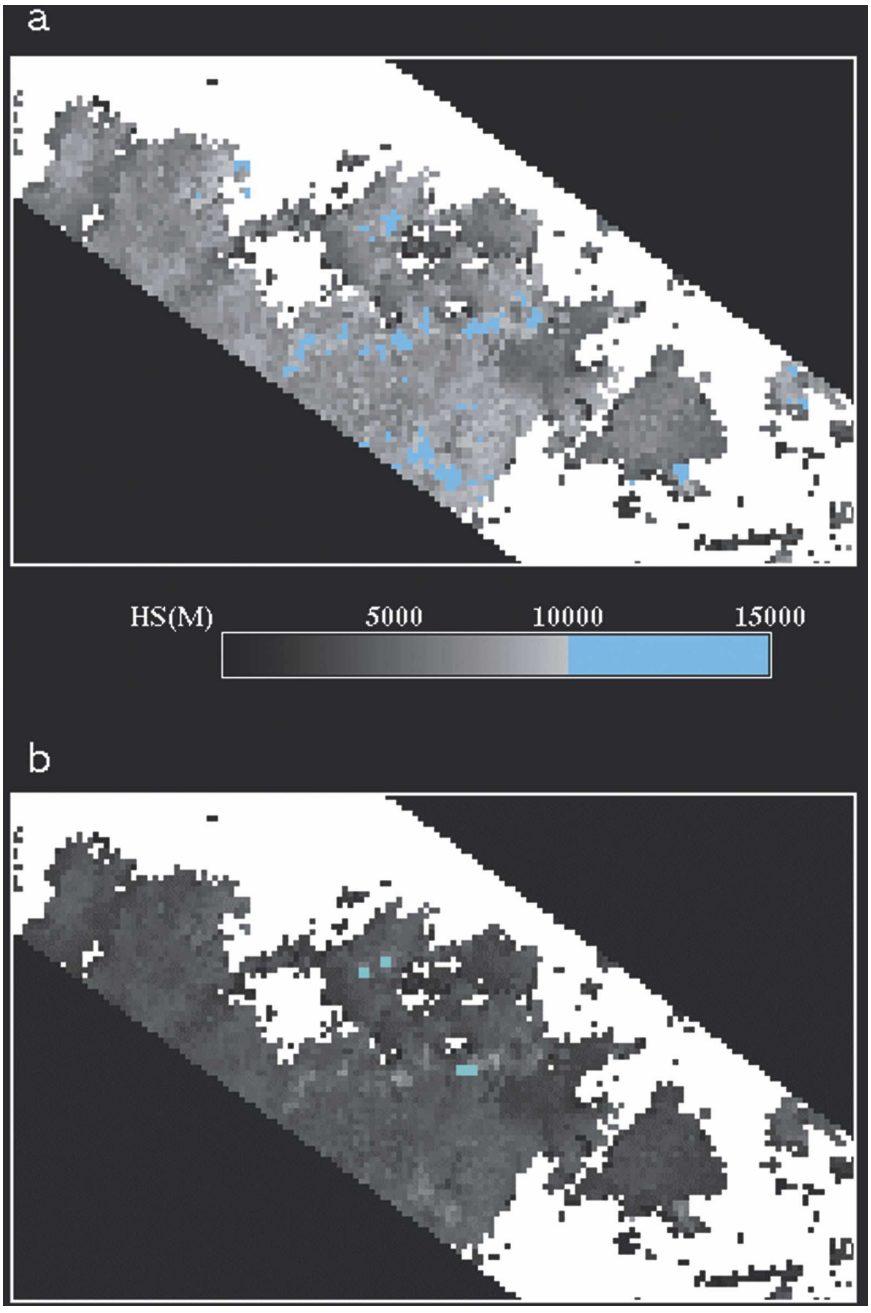

FIG. 5. Case-1 validation images from TRMM, where blue identifies (a) tower pixels (HS ≥ 10 000 m) or (b) nonzero event pixels (i.e., indicates lightning). The box marks the domain for this case. Within the domain, white indicates no rain and shades of gray represent HS.

b. Case 2

Early on the morning of 1 June 2003, *GOES-12* observed a convective system east of Cape Hatteras, North Carolina. The band-4 image (Fig. 7) shows the tail of a large comma cloud. A scalloped (undulated) rear edge indicates embedded cbs. The shape and orientation of the comma tail suggest a cold-frontal squall line (e.g., see Fig. 5.2.40 in Bader et al. 1995). As with case 1, the band-3 image (not shown) closely resembles the band-4 image, except in contrast. The domain selected for this case straddles the squall line and encloses the most prominent of the "backside" cbs, that is, the cb at 36°N, 72°W. Nowhere in the domain did band-4 temperature fall below 205 K.

A band trending southwest to northeast dominates

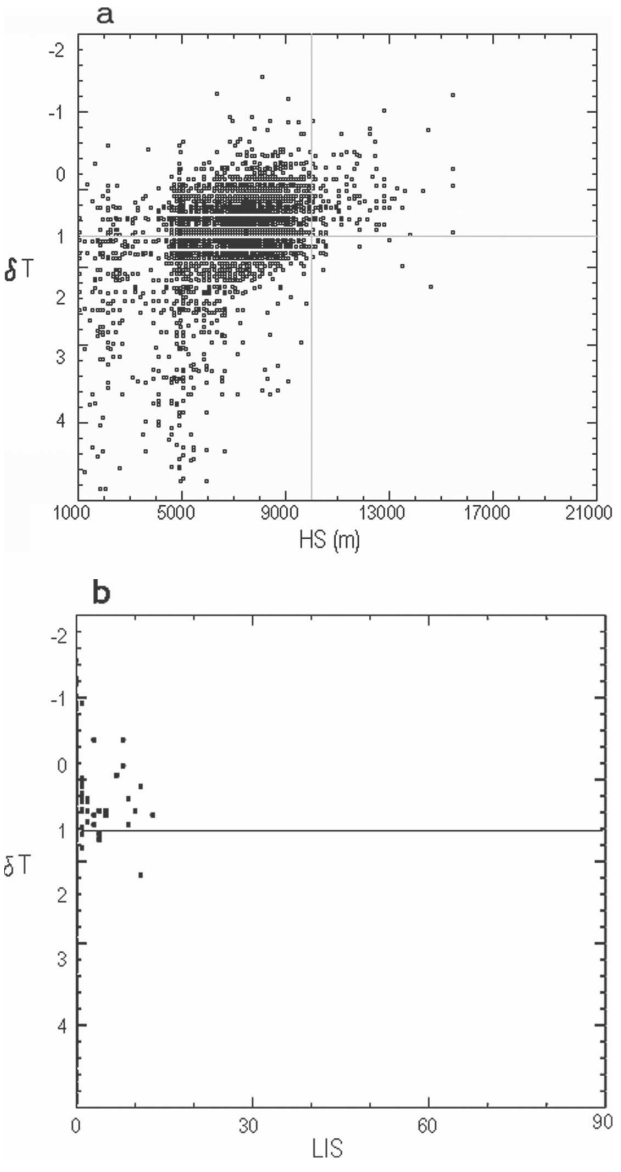

FIG. 6. Scatterplots for case 1, with δT_b as dependent variable and (a) HS or (b) event (LIS) as independent variable. The line at $\delta T_b = 1$ K delineates the space occupied by the nominal GCD (above) from that outside the nominal GCD (below). In (a), the line at HS = 10 000 m marks the cutoff for towers.

the brightness image (Fig. 8a). From east to west, the band spans nearly two-thirds of the domain. Brightness tends to decrease from the main backside cb eastward and southward. The δT_b sequence (Figs. 8b–h) begins with a small comma embedded within the brightness band. As δT_b decreases through the sequence, the small comma shrinks and corrodes. By the end of the δT_b sequence (Fig. 8h), it consists of scattered pixels and a few clumps of pixels. BMI (Fig. 8i) also shows a small comma. In size, position, and coherence, this comma most closely resembles the nominal-GCD comma (Fig. 8b).

TABLE 4. Statistics for case 1. The variables under the column headed "Statistic" are defined in appendix B. Here, δT_b is expressed in kelvins. The column headed "1" gives statistics for the nominal GCD. Case 1 has 8604 pixels.

	δT_b							
Statistic	1	0.5	0.25	0	−0.25	−0.5	−1	BMI
YY	144	126	108	85	65	47	25	157
YN	3435	2325	1681	1008	700	452	136	4311
NN	5009	6119	6763	7436	7744	7992	8308	4133
NY	16	34	52	75	95	113	135	3
Bias	2236	1531	1118	683	478	311	100	2792
POD_y	90	78	67	53	40	29	15	98
POD_n	59	72	80	88	91	94	98	48
FAR	95	94	93	92	91	90	84	96
CSI	4	5	5	7	7	7	8	3
HSS	4	6	8	11	11	12	14	3

Box-and-whisker plots comparing case-2 δT_b with case-2 T_b^{ir} (Fig. 9) show a finger much like that of case 1 (Fig. 4). The case-2 finger differs in two main respects. First, the axis of the finger drops into GCD space ($\delta T_b < 1$) at a slightly warmer value of T_b^{ir}. Second, reflecting differences in minimum band-4 temperatures, by about 10 K the case-2 finger is shorter than the case-1 finger.

Like GOES, the PR observed a band trending southwest to northeast (Fig. 10a). However, the HS band spans less than one-half of the width of the domain and lies mainly to the west of the center of the domain. A line of cells lies just within the western edge of the band. The most prominent of these cells coincides with the main backside cb in the brightness image (Fig. 8a).

Towers in HS (Fig. 10a) suggest two lines of cells, both aligned along the axis of the HS band. The line to the east consists of small (pixel and double pixel) cells. The line to the west includes the cell associated with the main backside cb. Tower cells nearly all fall within the nominal GCD (Fig. 8b). As with case 1, tower brightness pixels constituted a small sample of brightness pixels. For case 2, tower brightness includes most temperature-difference pixels brighter than 158 counts (δT_b of −2.4 K) and no pixels darker than 90 counts (δT_b of 2.9 K).

In clustering and in associations with HS peaks, events for case 2 (Fig. 10b) resembled those for case 1. However, event clusters in case 2 numbered four rather than two, and each contained scores rather than tens of pixels. These differences may reflect differences between the structure of a cell in a squall line (case 2) and in a cloud cluster (case 1) (e.g., Rys and Waldvogel 1986).

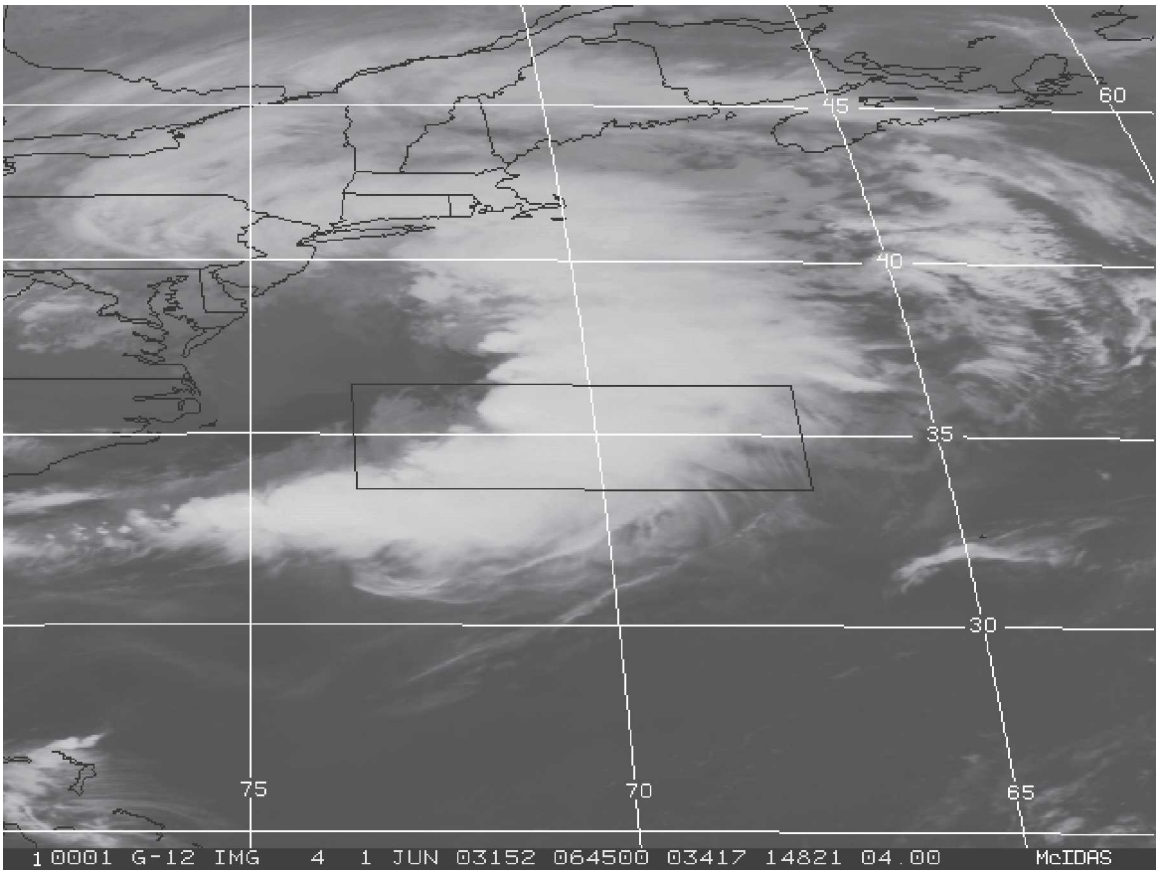

FIG. 7. Window infrared (band 4) GOES images for case 2, 0645 UTC 1 Jun 2003. The box centered at 35°N, 70°W marks the domain.

Figure 11a shows the scatterplot of HS and δT_b for case 2. Again, the point cloud forms a mushroom. However, the cap of the case-2 mushroom (especially for large HS) tilts less than does the cap of the case-1 mushroom. Less tilt in this quadrant of the graph implies a weaker relationship (no correlation) between tall echoes and δT_b.

In contrast with case 1, the scatterplot of LIS events and δT_b for case 2 (Fig. 11b) shows values up to 80, a number of events outside the nominal GCD space, and marked wedging. On the whole, the case-2 distribution of points much more closely conforms to the ideal pattern.

As in case 1, the nominal GCD overforecasts (Table 5). In a similar way, POD_y drops and POD_n rises as δT_b decreases. At all thresholds, case 2 exhibits higher bias and higher FAR than does case 1. Except at a δT_b of -1, case-2 GCD detects a smaller fraction of tower pixels. However, at all thresholds below a δT_b of $+0.5$, case-1 GCD detects a larger fraction of POD_n pixels. The skill indices reflect these differences. Case-2 CSI scores run from one-third to one-half of those of case 1; case-2 Heidke skill scores run from one-third to three-quarters of those of case 1. Performance tends to improve as δT_b decreases.

At all levels, the benchmark index beats the experimental GCD in detecting tower pixels. False-alarm rates are about equal whatever the value of δT_b is. In terms of skill scores, BMI matches the performance of the nominal GCD and first two experimental GCDs. For $\delta T_b < 0.5$ K, the experimental GCD tends to perform better than the BMI.

c. *Composite results*

Maps of GCD at the nominal threshold tended to show blobs, typically one per case. At progressively smaller values of δT_b, each blob tended to shrink and fray. In all cases, the nominal GCD blob for a case encompassed most of the corresponding tower pixels.

For the nominal threshold of δT_b $(+1)$ and for two experimental thresholds (0 and -1), Table 6 presents statistics for each of the six maritime cases (1–6). At the nominal threshold one case (4) yielded less than 15 YY pixels, at the zero threshold two additional cases (5 and

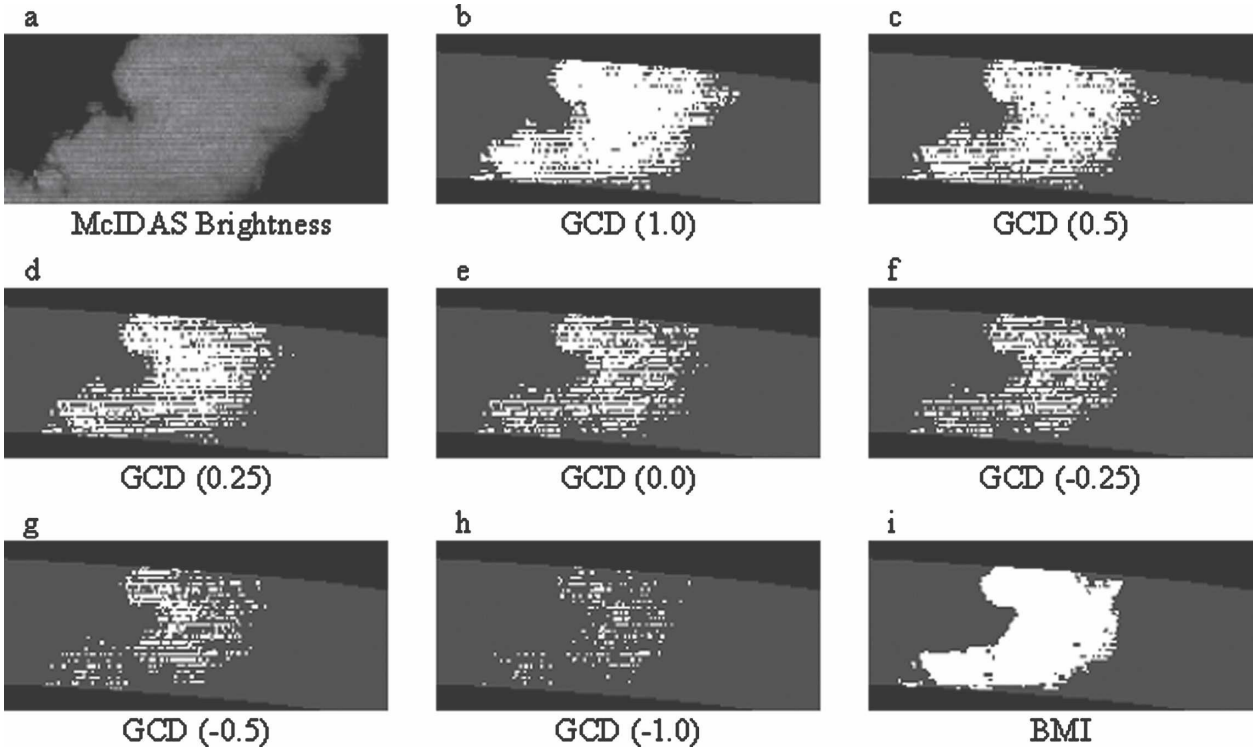

FIG. 8. Case-2 GOES image products for the domain, each in rectilinear projection: (a) McIDAS brightness, (b) nominal GCD, (c)–(h) experimental GCD, and (i) BMI.

6) yielded less than 15 YY pixels, and at the −1 threshold yet another case (2) yielded less than 15 YY pixels. Small samples in the yes–yes quadrant decrease confidence in the performance statistics.

This caution notwithstanding, at the nominal threshold performance fell below our expectation. In all cases, the false-alarm rate exceeds 85%. Except for case 3, good detection of one category of pixel means poor detection of the other. No skill score exceeds 13%. In terms of CSI and HSS, case 2 ranks fifth from the top and case 1 ranks third or fourth from the top.

By most measures, two of the six maritime cases stand out. Case 6 demonstrates no skill, and case 3 demonstrates skill at the 11%–13% level. Case 6 was a tropical storm (Bill) crossing the Louisiana coast. Shadows (in the visible image—not shown) and coincident cold spots indicate (at best) narrow, shallow overshooting tops. Band-4 temperatures are as low as 198 K. Within the domain, the PR measured towers to 16.6 km. However, towers occupy fewer than 30 pixels. Along the Gulf Coast, *Storm Data* (NCDC 2003) notes only flooding (no severe convective weather) in the hours near and after the case-6 scan-time coincidence.

Case 3 occurred on the opposite side of the Gulf of Mexico. Case 3 is a compact nocturnal cloud cluster and has band-4 temperatures as low as 189 K. Echo heights peak at 17 km; the count of towers exceeds 260.

At the zero-threshold level, the false-alarm rate remains high. For all cases, good detection of one category of pixel means poor detection of the other. Cases 3 and 6 still stand out as, respectively, best and worst. However, bias improves markedly, and for most cases skill scores at the zero-threshold level are higher than skill scores at the nominal-threshold level.

Marginally (in an absolute sense), performance improves for case 2 from a threshold of 1 to a threshold of

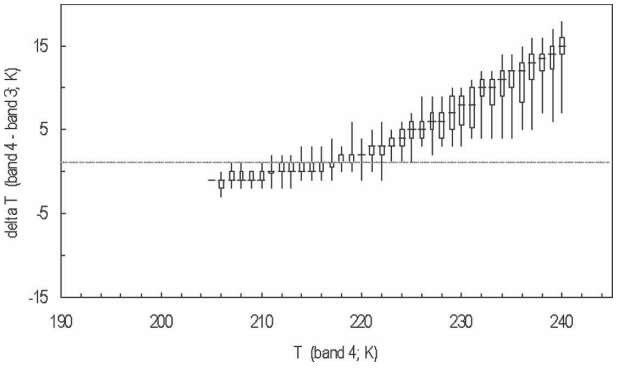

FIG. 9. Box-and-whisker plots for case 2.

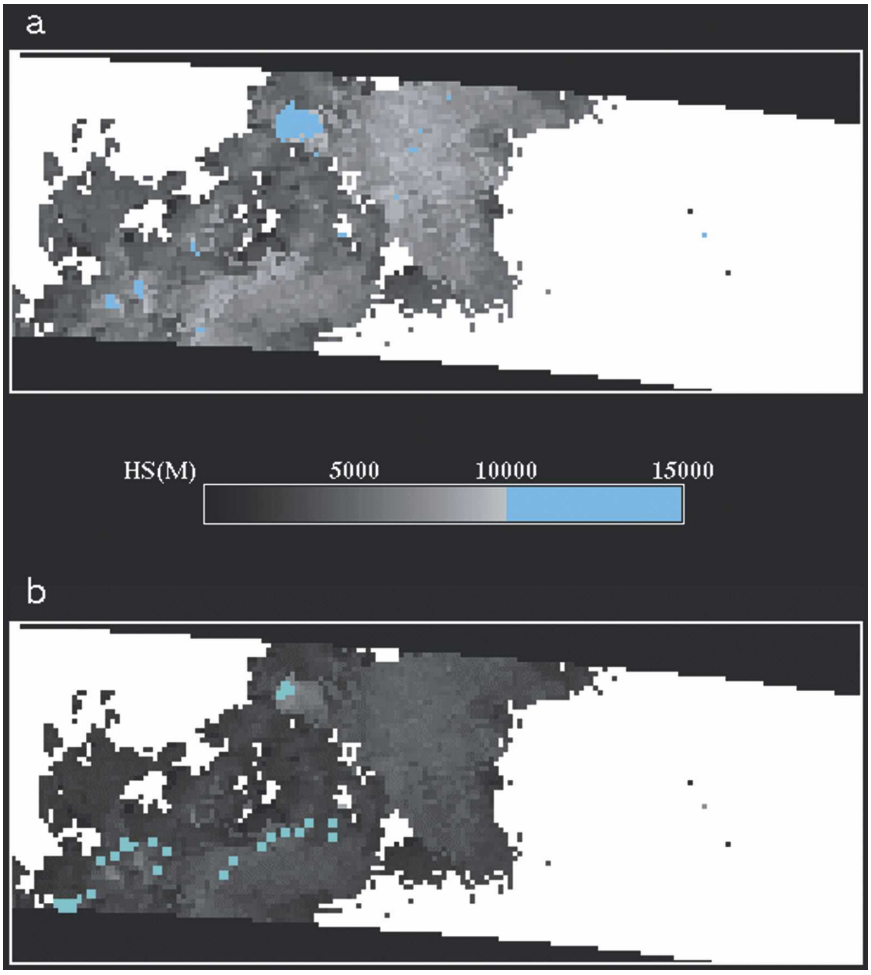

FIG. 10. Case-2 validation images from TRMM, where blue identifies (a) tower pixels or (b) event pixels.

0. However, performance improves substantially for case 1. At the zero-threshold level, case 2 ranks sixth from the top and case 1 ranks third or fourth from the top.

Ignoring cases 4 and 5, we find that from the 0 threshold to the −1 threshold the bias score continues to improve. Except for case 3, this change drives skill scores upward. The improvement is most notable for case 1, which (at the −1 threshold) has the highest skill scores.

Table 6 also presents statistics for case 7. With respect to skill scores at the nominal threshold, case 7 stands out from each of the maritime cases. In this case alone, dropping the threshold consistently diminishes performance. Case 7 was a Great Plains squall line. Overshooting tops in the *GOES-12* visible image and enhanced-Vs in the *GOES-12* infrared image indicate strong updrafts within the cells. Cloud-top temperatures are as cold as 200 K. The PR measured echo heights to 17.5 km. Towers occupy 1200 pixels. For western, central, and southeastern Oklahoma and northern Texas, *Storm Data* (NCDC 2003) lists several reports of hail and damaging winds in the 1-h window centered on the case-7 scan-time coincidence. Viewed at infrared wavelengths by *GOES-12*, case 7 differs from case 2 in three main respects: smaller anvils, colder temperatures, and enhanced-Vs imprinted on the tops of a few of the anvils.

As with the band-4 statistics [section 3b(3)], threshold by threshold, GCD composite cases were constructed from the GCD maritime contingency tables. Table 7 and Fig. 12 present the results. For the nominal GCD we find skill scores of ~5% and somewhat high bias and FAR (Table 7). Except for POD_y (the probability of detecting a tower pixel), performance tends to improve as the δT_b threshold drops from +1 to −0.5. Although modest in absolute terms, the change amounts to a 50%–100% improvement in skill scores.

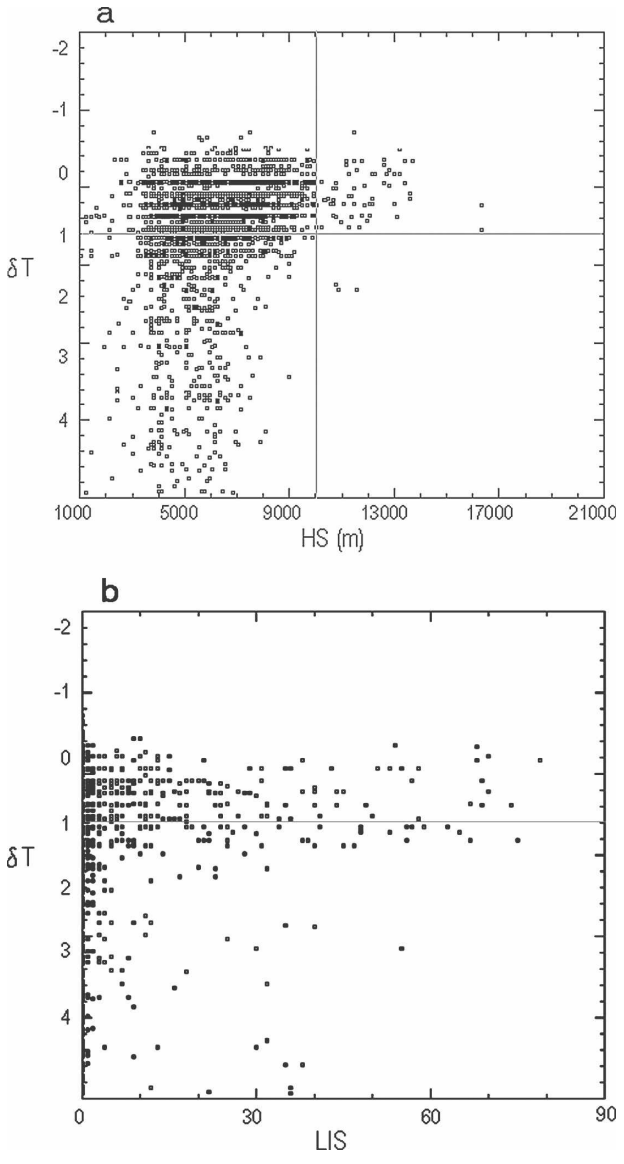

FIG. 11. Scatterplots for case 2, where the independent variable is (a) HS or (b) event (LIS).

TABLE 5. Statistics for case 2. Conventions are as in Table 4. Case 2 has 10 666 pixels.

	δT_b							
Statistic	1	0.5	0.25	0	−0.25	−0.5	−1	BMI
YY	80	72	65	49	38	32	13	74
YN	3634	2957	2316	1544	1338	889	339	3130
NN	6948	7625	8266	9038	9244	9693	10 243	7452
NY	4	12	19	35	46	52	71	10
Bias	4421	3605	2834	1896	1638	1096	419	3814
POD_y	95	85	77	58	45	38	15	88
POD_n	65	72	78	85	87	91	96	70
FAR	97	97	97	96	97	96	96	98
CSI	2	2	2	3	2	3	3	2
HSS	3	3	4	4	4	5	5	3

Marginally, BMI (Table 7, right-hand column) beats GCD at the nominal threshold. It detects more than 90% of the tower pixels but issues false alarms at a rate of more than 95%.

Figure 12 contrasts the distributions of echo heights for the two classes of GCD pixels (cb and not-cb). Each pair of distributions (cb and not-cb) includes all "echo" pixels in the composite case. Consider the pair of curves representing the nominal GCD (solid lines). In relation to one another, the cb distribution is flat and the not-cb distribution is peaked. Also, despite considerable overlap, the cb distribution lies toward the high-HS end of the scale and the not-cb distribution lies toward the low-HS end of the scale. This pattern conforms to the behavior indicated in Figs. 6a and 11a.

Dropping the GCD threshold from 1 to 0 changes the shapes of the distributions more than the positions. For cb pixels, the distribution flattens; for not-cb pixels, it sharpens. The effect of the changes is to sharply reduce the number of false positives and to modestly reduce the number of true positives (also see Table 7). Dropping the GCD threshold from 0 to −0.5 (not shown) continues this trend, but at a lesser rate.

At the +1 threshold, the mean HS is ~5.3 and ~1.5 km for cb and not-cb pixels, respectively. Whether for cb or not-cb categories, at each successive threshold step, mean HS increases. Increases occur in lockstep. Thus, the category difference in mean HS remains essentially the same (3.7–3.8 km) for each threshold.

We might propose three conditions for the selection of an optimum δT_b threshold: first, skill scores that are significantly better than those of BMI; second, a high probability (>50%) of detecting a tower pixel; and, third, nonzero skill across a range of convective systems. For the six maritime cases considered here, these conditions lead to an optimum δT_b of approximately 0.

5. Concluding remarks

We describe a test of GCD performance over the tropical and subtropical northwestern Atlantic and northeastern Pacific Oceans. Drawing on *GOES-12* image data, the test targeted individual convective systems but operated on pixels rather than on convective entities. Height-of-storm measurements from the TRMM precipitation radar and flash counts from the TRMM Lightning Imaging Sensor served as validation data.

For a 6-week period beginning in mid-May 2003, passes of the PR were matched in time and space to

TABLE 6. Case statistics for three values of δT_b. Numbers in parentheses give sample sizes. Otherwise, conventions follow those in Table 4.

		Case						
δT_b	Statistic	1 (8604)	2 (10 666)	3 (5745)	4 (10 039)	5 (10 188)	6 (8046)	7 (8034)
1	YY	144	80	211	6	19	24	776
	YN	3435	3634	1635	573	480	2578	675
	NN	5009	6948	3846	9457	9673	5442	6166
	NY	16	4	53	3	16	2	417
	Bias	2236	4421	699	6433	1425	10 007	121
	POD_y	90	95	79	66	54	92	65
	POD_n	59	65	70	94	95	67	90
	FAR	95	97	88	98	96	99	46
	CSI	4	2	11	1	3	0	41
	HSS	4	3	13	2	7	1	51
0	YY	85	49	142	6	9	14	172
	YN	1008	1544	1044	136	86	981	55
	NN	7436	9038	4437	9894	10 067	7039	6786
	NY	75	35	122	3	26	12	1021
	Bias	683	1896	449	1577	271	3826	19
	POD_y	53	58	53	66	25	53	14
	POD_n	88	85	80	98	99	87	99
	FAR	92	96	88	95	90	98	24
	CSI	7	3	10	4	7	1	13
	HSS	11	4	13	8	13	2	20
−1	YY	25	13	54	1	0	7	18
	YN	136	339	446	13	12	169	3
	NN	8308	10 243	5035	10 017	10 141	7851	6838
	NY	135	71	210	8	35	19	1175
	Bias	100	419	189	155	34	676	1
	POD_y	15	15	20	11	0	26	1
	POD_n	98	96	91	99	99	97	99
	FAR	84	96	89	92	100	96	14
	CSI	8	3	7	4	0	3	1
	HSS	14	5	9	9	0	6	2

images from *GOES-12*. In 11 of the 55 matches, the time–space window of coincidence framed all or part of a convective system. Six of these systems were selected for analysis. These six cases included two cloud clusters, two vortical clouds, one squall line, and a landfalling tropical storm.

Two of the six cases were examined in detail. In neither case did the statistical character of the distribution of brightness temperature difference (window − water vapor) as a function of infrared brightness temperature differ significantly from that reported for the global tropics and midlatitudes. Maps of GCD at the nominal

TABLE 7. Statistics for the composite case. Conventions are as in Table 4. Pixel count is 53 288.

	δT_b							
Statistic	1	0.5	0.25	0	−0.25	−0.5	−1	BMI
YY	484	419	375	305	248	198	100	538
YN	12 335	9162	7164	4799	3759	2601	1115	13 231
NN	40 375	43 548	45 546	47 911	48 951	50 109	51 595	39 479
NY	94	159	203	273	330	380	478	40
Bias	2218	1658	1304	883	693	484	210	2382
POD_y	84	72	65	53	43	34	17	93
POD_n	77	83	86	91	93	95	98	75
FAR	96	96	95	94	94	93	92	96
CSI	4	4	5	6	6	6	6	4
HSS	5	6	7	9	9	10	10	6

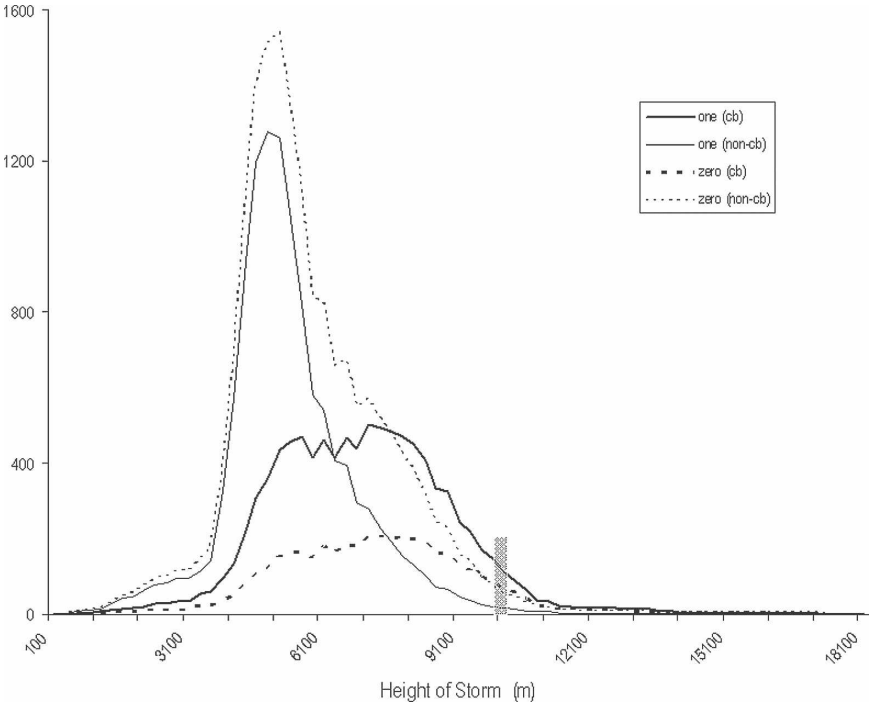

FIG. 12. The cb and not-cb frequency distributions of echo height (HS) for the nominal GCD (1 K; solid lines) and one of the experimental GCDs (0 K; dashed lines). Both pairs of distributions (1 and 0) refer to the composite case. Values were binned at a resolution of 250 m across the interval from 100 to 18 350 m. Each distribution is smoothed by a five-point running mean. The bar near the midpoint of the x axis marks the bin containing the threshold (10 000 m) for tower echoes.

threshold of difference in brightness temperature tended to show blobs. At progressively smaller values of the δT_b threshold, each blob tended to shrink and fray.

The nominal GCD (threshold of +1) consistently predicted too many deep-convective pixels. For most convective systems, skill scores improved as the δT_b threshold was dropped from 1 to 0. At this threshold the false alarm ratio ranged from 88% to 98% and the Heidke skill score ranged from 2% to 13%. At this threshold, too, the algorithm consistently outperformed a single-threshold (215 K), infrared-only index. We tentatively conclude that the GCD—especially at thresholds lower than the nominal value—offers the community a new tool for detecting and mapping deep cumulus convection over the oceans.

Among unresolved issues, four stand out. First, GCD performance varied considerably from case to case. Second, the present results may apply only to convective systems occurring over the ocean. Third, the results might be different for some other geostationary satellite. Last, results with the LIS suggest value in incorporating information from lightning sensors. In anticipation of instruments on future generations of geostationary satellites, in a subsequent study we plan to adapt the GCD to accept lightning data.

Acknowledgments. The HS data from the PR were acquired from the DAAC at the National Aeronautics and Space Administration (NASA) Goddard Space Flight Center (information was available online at http://daac.gsfc.nasa.gov/). Event data were obtained from NASA's Marshall Space Flight Center, through the Global Hydrology Resource Center (information was available online at http://thunder.msfc.nasa.gov/data/). TRMM is an international project that is jointly sponsored by the Japan Aerospace Exploration Agency (JAXA) and NASA. The authors appreciate the thoughtful comments of the reviewers.

APPENDIX A

Definition of the Variables 34DF and McIDAS Brightness

The difference variable, δT_b, ranges across the value 0. To achieve a useful McIDAS display, a new variable, 34DF, was defined:

$$\text{If} \quad |\delta T_b| \le 10\ \text{K}, \quad \text{then} \quad 34\text{DF} = -20\delta T_b,$$
$$\text{else} \quad 34\text{DF} = 0. \tag{A1}$$

Then, 8-bit McIDAS brightness was related to 34DF:

$$\text{If} \quad |34\text{DF}| \le 200, \quad \text{then}$$
$$\text{McIDAS brightness} = (255/400)(34\text{DF} + 200), \quad \text{else}$$
$$\text{McIDAS brightness} = 0. \tag{A2}$$

APPENDIX B

Formulas Used to Calculate the Validation Statistics Listed in Table 2

Given some case, we express the performance of the diagnostic scheme (GCD or BMI) in terms of a 2×2 contingency table (cf. Mahoney et al. 2000). In this table, the y axis is the HS tower (the "observed" value) and the x axis is either GCD or BMI (the "predicted" value). Then, YY is predicted cb and observed cb, YN is predicted cb and observed not-cb, NN is predicted not-cb and observed not-cb, and NY is predicted not-cb and observed cb. Various combinations of these variables yield the following statistics:

$$\text{bias} = 100(\text{YY} + \text{YN})/(\text{YY} + \text{NY}),$$
$$\text{POD}_y = 100 \times \text{YY}/(\text{YY} + \text{NY}),$$
$$\text{POD}_n = 100 \times \text{NN}/(\text{YN} + \text{NN}),$$
$$\text{FAR} = 100 \times \text{YN}/(\text{YY} + \text{YN}),$$
$$\text{CSI} = 100 \times \text{YY}/(\text{YY} + \text{NY} + \text{YN}), \quad \text{and}$$
$$\text{HSS} = 100[(\text{YY} + \text{NN}) - c]/[(\text{YY} + \text{YN} + \text{NY} + \text{NN}) - c],$$

where

$$c = [(\text{YY} + \text{YN})(\text{YY} + \text{NY}) + (\text{NY} + \text{NN})(\text{YN} + \text{NN})]/(\text{YY} + \text{YN} + \text{NY} + \text{NN}).$$

REFERENCES

Ackerman, S. A., 1996: Global satellite observations of negative brightness temperature differences between 11 and 6.7 μm. *J. Atmos. Sci.,* **53,** 2803–2812.

Adler, R. F., M. J. Markus, and D. D. Fenn, 1985: Detection of severe Midwest thunderstorms using geosynchronous satellite data. *Mon. Wea. Rev.,* **113,** 769–781.

Ba, M. B., and A. Gruber, 2001: GOES Multispectral Rainfall Algorithm (GMSRA). *J. Appl. Meteor.,* **40,** 1500–1514.

Bader, M. J., G. S. Forbes, R. B. E. Lilley, and A. J. Waters, 1995: *Images in Weather Forecasting: A Practical Guide for Interpreting Satellite and Radar Imagery*. Cambridge University Press, 499 pp.

Brennan, W. T., 1983: Thunderstorms. Federal Aviation Administration Advisory Circular 00-24B, 8 pp. [Available online at http://www.airweb.faa.gov/Regulatory_and_Guidance_Library/rgAdvisoryCircular.nsf/MainFrame?OpenFrameSet.]

Christian, H. J., R. J. Blakeslee, S. J. Goodman, and D. M. Mach, 2000: Algorithm theoretical basis document (ATBD) for the Lightning Imaging Sensor (LIS). NASA/Marshall Space Flight Center, 53 pp. [Available online at http://thunder.msfc.nasa.gov/bookshelf/.]

Ebert, E. E., M. J. Manton, P. A. Arkin, R. J. Allam, C. E. Holpin, and A. Gruber, 1996: Results from the GPCP Algorithm Intercomparison Programme. *Bull. Amer. Meteor. Soc.,* **77,** 2875–2887.

Ellrod, G. P., R. V. Achutuni, J. M. Daniels, E. M. Prins, and J. P. Nelson III, 1998: An assessment of *GOES-8* imager data quality. *Bull. Amer. Meteor. Soc.,* **79,** 2509–2526.

Frank, N. L., and H. M. Johnson, 1969: Vortical cloud systems over the tropical Atlantic during the 1967 hurricane season. *Mon. Wea. Rev.,* **97,** 124–129.

Fritz, S., and I. Laszlo, 1993: Detection of water vapor in the stratosphere over very high clouds in the tropics. *J. Geophys. Res.,* **98,** 22 959–22 967.

Fu, R., A. D. Del Genio, and W. B. Rossow, 1990: Behavior of deep convective clouds in the tropical Pacific deduced from ISCCP radiances. *J. Climate,* **3,** 1129–1152.

Gifford, F. A., 1989: The shape of large tropospheric clouds, or "very like a whale." *Bull. Amer. Meteor. Soc.,* **70,** 468–475.

Jordan, C. L., 1958: Mean soundings for the West Indies area. *J. Meteor.,* **15,** 91–97.

Kozu, T., and Coauthors, 2001: Development of precipitation radar onboard the Tropical Rainfall Measuring Mission (TRMM) satellite. *IEEE Trans. Geosci. Remote Sens.,* **39,** 102–116.

Kuligowski, R. J., 2002: A self-calibrating real-time GOES rainfall algorithm for short-term rainfall estimates. *J. Hydrometeor.,* **3,** 112–130.

Kurino, T., 1997: A satellite infrared technique for estimating "deep/shallow" precipitation. *Adv. Space Res.,* **19,** 511–514.

Laing, A. G., and J. M. Fritsch, 1993: Mesoscale convective complexes in Africa. *Mon. Wea. Rev.,* **121,** 2254–2263.

Lane, T. P., R. D. Sharman, T. L. Clark, and H.-M. Hsu, 2003: An investigation of turbulence generation mechanisms above deep convection. *J. Atmos. Sci.,* **60,** 1297–1321.

Lau, K. M., T. Nakazawa, and C. H. Sui, 1991: Observations of cloud cluster hierarchies over the tropical western Pacific. *J. Geophys. Res.,* **96,** 3197–3208.

Lazzara, M. A., and Coauthors, 1999: The Man computer Interactive Data Access System: 25 years of interactive processing. *Bull. Amer. Meteor. Soc.,* **80,** 271–284.

Liou, K. N., S. C. Ou, Y. Takano, F. P. J. Valero, and T. P. Ackerman, 1990: Remote sounding of the tropical cirrus cloud temperature and optical depth using 6.5 and 10.5 μm radiometers during STEP. *J. Appl. Meteor.,* **29,** 716–726.

Mahoney, J. L., B. G. Brown, and J. E. Hart, 2000: Statistical verification results for the Collaborative Convective Forecast Product. NOAA Tech. Rep. OAR 457-FSL 6, Boulder, CO, 30 pp. [Available online at http://www-ad.fsl.noaa.gov/fvb/publications/articles/ccfp_statistical_results_2000.pdf.]

Mapes, B. E., and R. A. Houze, 1993: Cloud clusters and superclusters over the oceanic warm pool. *Mon. Wea. Rev.,* **121,** 1398–1416.

Mosher, F. R., 2001: A satellite diagnostic of global convection. Preprints, *11th Conf. on Satellite Meteorology,* Madison, WI, Amer. Meteor. Soc., 416–419.

——, 2002: Detection of deep convection around the globe. Pre-

prints, *10th Conf. on Aviation, Range, and Aerospace Meteorology,* Portland, OR, Amer. Meteor. Soc., 289–292.

NCDC, 2003: *Storm Data*. Vol. 45, No. 6, 386 pp.

Ottenbacher, A., and J. Schmetz, 1994: Relationship of collocated cloud radiances in the Meteosat IR and WV channel. *Passive Infrared Remote Sensing of Clouds and the Atmosphere II,* D. K. Lynch, Ed., International Society for Optical Engineering (SPIE Proceedings Vol. 2309), 45–51.

Rys, F. S., and A. Waldvogel, 1986: Fractal shape of hail clouds. *Phys. Rev. Lett.,* **56,** 784–787.

Schmetz, J., S. A. Tjemkes, M. Gube, and L. van de Berg, 1997: Monitoring deep convection and convective overshooting with Meteosat. *Adv. Space Res.,* **19,** 433–441.

Sherwood, S. C., and R. Wahrlich, 1999: Observed evolution of tropical deep convective events and their environment. *Mon. Wea. Rev.,* **127,** 1777–1795.

Szejwach, G., 1982: Determination of semi-transparent cirrus cloud temperature from infrared radiances: Application to Meteosat. *J. Appl. Meteor.,* **21,** 384–393.

Tjemkes, S. A., L. van de Berg, and J. Schmetz, 1997: Warm water vapour pixels over high clouds as observed by Meteosat. *Beitr. Phys. Atmos.,* **70,** 15–21.

Weinreb, M. P., J. X. Johnson, and D. Han, cited 2006: Conversion of GVAR infrared data to scene radiance or temperature. NOAA NESDIS Office of Satellite Operations. [Available online at http://www.oso.noaa.gov/goes/goes-calibration/gvar-conversion.htm.]

Wylie, D. P., D. Santek, and D. O'C. Starr, 1998: Cloud-top heights from *GOES-8* and *GOES-9* stereoscopic imagery. *J. Appl. Meteor.,* **37,** 405–413.

Zhang, C., 1993: On the annual cycle in highest, coldest clouds in the tropics. *J. Climate,* **6,** 1987–1990.